An introduction to combined Fourier–wavelet transform and its application to convectively coupled equatorial waves

Kazuyoshi Kikuchi

Abstract Convectively coupled equatorial waves (CCEWs) are major sources of tropical day-to-day variability. The majority of CCEWs-related studies for the past decade or so have based their analyses, in one form or another, on the Fourier-based space–time spectral analysis method developed by Wheeler and Kiladis (WK). Like other atmospheric and oceanic phenomena, however, CCEWs exhibit pronounced nonstationarity, which the conventional Fourier-based method has difficulty elucidating. The purpose of this study is to introduce an analysis method that is able to describe the time-varying spectral features of CCEWs. The method is based on a transform, referred to as the combined Fourier–wavelet transform (CFWT), defined as a combination of the Fourier transform in space (longitude) and wavelet transform in time, providing an instantaneous space–time spectrum at any given time. The elaboration made on how to display the CFWT spectrum in a manner analogous to the conventional method (i.e., as a function of zonal wavenumber and frequency) and how to estimate the background noise spectrum renders the method more practically feasible. As a practical example, this study analyzes 3-hourly cloud archive user service (CLAUS) cloudiness data for 23 years. The CFWT and WK methods exhibit a remarkable level of agreement in the distributions of climatological-mean space–time spectra over a wide range of space–time scales ranging in time from several hours to several tens of days, indicating the instantaneous CFWT spectrum provides a reasonable snapshot. The usefulness of the capability to localize space–time spectra in time is demonstrated through examinations of the annual cycle, interannual variability, and a case study.

Keywords Convectively coupled equatorial waves · Tropical convection · Wavelet · Annual cycle · Interannual variability

1 Introduction

Organized deep convection in the tropics is usually a manifestation of equatorially trapped large-scale atmospheric wave motions (Matsuno 1966) coupled with convection, collectively referred to as convectively coupled equatorial waves (CCEWs) (see Kiladis et al. 2009 for a review). They exhibit a broad spectrum of space–time scales (as shown later it spans in time from several hours to a few tens of days) and are responsible for a large proportion of day-to-day weather variability in the tropics.

Overall, CCEWs have multifaceted roles in weather and climate. They are among the major building blocks of the climatological intertropical convergence zone (ITCZ), especially in the Pacific and Atlantic sectors (e.g., Serra and Houze 2002; Roundy and Frank 2004; Mounier et al. 2007), and some of which are also the major building blocks of the Madden–Julian oscillation (MJO) (e.g., Nakazawa 1988; Kikuchi and Wang 2010; Yang and Ingersoll 2011). Certain types of CCEWs have a profound influence on the frequency of tropical cyclogenesis in various basins (e.g., Frank and Roundy 2006; Schreck et al. 2012). In addition, they are a significant source of upward propagating waves into the stratosphere that drive the quasi-biannual oscillation (QBO) (e.g., Baldwin et al.

K. Kikuchi (✉)
International Pacific Research Center, School of Ocean and Earth Science and Technology, University of Hawaii at Mānoa, 1680 East West Road, POST Bldg. 401, Honolulu, HI 96822, USA
e-mail: kazuyosh@hawaii.edu

2001; Kawatani et al. 2010). Thus, an in-depth understanding of spatial and temporal variations of CCEWs is essential for a complete understanding of many parts of the weather/climate system.

Over the last few decades, detection and identification of CCEWs have been relied heavily on Fourier transform (FT)-based space–time spectral analysis of satellite-derived cloudiness or rainfall data. Takayabu (1994) was the first to conduct such spectral analysis making use of relatively high resolution cloudiness data over the western Pacific. In their seminal paper, built on the work of Takayabu (1994), Wheeler and Kiladis (1999) developed a more sophisticated method by taking into account a set of practical considerations including data handling and statistical assessment of space–time spectral peaks. At present the method seems to be widely accepted as the standard method.

Such FT-based spectral methods, however, have limitations in their applicability to a nonstationary signal (i.e., whose statistical properties vary with time). In the FT, a signal is represented as a series of sine and cosine functions of different frequencies. The corresponding Fourier coefficients are evaluated over some prescribed interval, giving rise to the "global" spectrum representing energy contributions from processes with different frequencies (i.e., timescales) made over the interval. It is clearly apparent that the FT is fully functional as long as the signal is stationary, while if the signal is nonstationary it does only a poor job as it does not provide any clue as to how the spectral properties vary with time within the interval. Like any other phenomena observed in the Earth system, CCEWs are, in essence, nonstationary. Presumably, their statistical properties change on various timescales, which are in principle dependent on the more slowly-varying atmospheric-ocean background state, regulated by the MJO, annual cycle, and interannual variability, and among others.

The wavelet transform (WT), appeared in the 1980s, has been used in a rich variety of disciplines. In contrast to the FT, a signal is represented as a series of time localized wave packets of different scales. The corresponding wavelet coefficients, a measure of the degree of similarity between the signal and the individual wave packets, are determined locally, providing the "local" spectrum representing energy contributions from processes with different frequencies made at a specific time. The usefulness of the WT in analyzing a variety of phenomena in the geophysical and atmospheric sciences has been proved over the last two decades (Hudgins et al. 1993; Lau and Weng 1995; Kumar and FoufoulaGeorgiou 1997; Torrence and Compo 1998; Yano et al. 2001; Labat 2005).

As for its application to CCEWs, its two-dimensional versions (i.e., based on a set of spatially as well as temporally localized wave packets) have been used in some recent studies (Wong 2009; Kikuchi and Wang 2010; Roundy 2012; Roundy and Janiga 2012). Kikuchi and Wang (2010) used the so-called spatio-temporal WT (STWT), specifically designed to analyze space–time signals and well suited for motion analysis (Duval-Destin and Murenzi 1993), and demonstrated its usefulness in examining the interrelationships between the MJO and CCEWs. Their preliminary results appear promising, though it is computationally cumbersome and the information it provides is too comprehensive in some cases.

The purpose of this paper is to introduce a novel diagnostic tool, making use of the WT, for examining the nonstationarity in a two-dimensional space–time (in particular longitude–time) signal, which is computationally more feasible and generates more simple and succinct space–time spectra relative to the STWT. The transform is defined as a combination of the Fourier series in longitude and the WT in time (Fig. 1), referred to as the combined Fourier–wavelet transform (CFWT). It follows from its definition that the CFWT provides spatially global but temporally local (instantaneous) space–time spectra. The idea behind this combination is that the data is usually zonally periodic and, in many situations, we are more interested in the temporal variations in the spectrum than in the spatial variations. Note that the opposite combination (i.e., the WT in longitude and the FT in time) can be found in a previous study by Gu and Zhang (2001). Section 2 introduces the mathematical formulation of the CFWT and discusses its fundamental properties in their continuous form for simplicity, followed by a discussion of some practical issues. A series of examples are presented in Sect. 3 through its application to satellite-derived cloudiness data. Section 4 concludes this paper. Our focus is on the introduction to the method, although the results contain some interesting nonstationary features of CCEWs that would motivate further studies.

2 Combined Fourier–wavelet transform

2.1 Continuous CFWT

We begin by introducing the CFWT and its fundamental properties in continuous form. The CFWT is defined as a combination of the Fourier series in the zonal direction and the WT in the time direction as follows. Let $g(x, t)$ be a two dimensional signal as a function of x (longitude) and t (time). Here g is assumed to be zonally periodic. Note that for a zonally nonperiodic signal, the more general expression can be readily obtained by using the FT in place of the Fourier series.

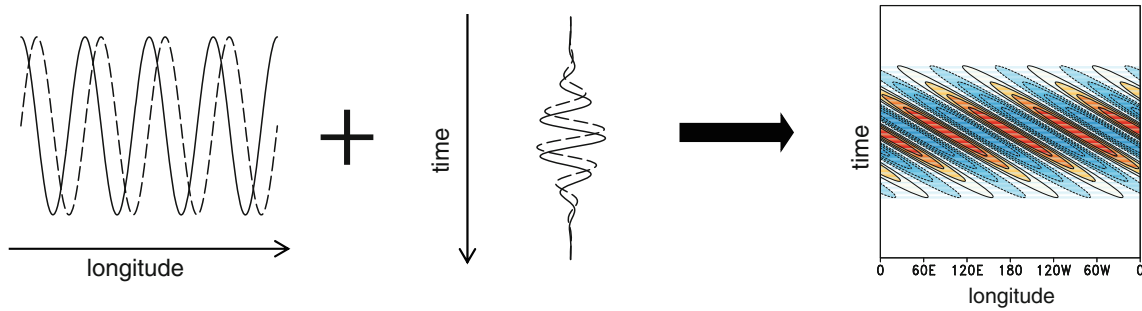The CFWT $\mathcal{T}$ of the function g is written as

Fig. 1 Schematic illustrating the concept of the CFWT, which is defined as a combination of the Fourier series in longitude and the WT in time. The combination of a complex exponential with a particular zonal wavenumber (*left*) and a complex wavelet with a particular wavelet scale (*middle*) gives rise to a time localized wave packet (*right*, the real part is only shown), which acts as a mold to measure the degree to which the longitude–time section of a signal at a given time is accounted for by this wave packet pattern. Real and imaginary parts are indicated by *solid* and *dashed lines*, respectively, in the *left* and *middle panels*

$$(\mathcal{T}g)(k,s,\tau) = \frac{1}{2\pi} \int_0^{2\pi} dx \int_{-\infty}^{\infty} g(x,t)\psi_{s,\tau}^*(t)e^{ikx}dt \qquad (1)$$

where ψ is a mother wavelet, $\psi_{s,\tau}(t) = |s|^{-1/2}\psi\{(t-\tau)/s\}$ is a dilated (denoted by the scale parameter $s \in \mathbb{R}$ and $s \neq 0$) and translated (denoted by the translation parameter $\tau = \mathbb{R}$) version of the mother wavelet, the asterisk denotes complex conjugate, and k zonal wave number. It can also be represented in the zonal wavenumber-frequency domain as

$$(\mathcal{T}g)(k,s,\tau) = |s|^{1/2} \int_{-\infty}^{\infty} \widehat{\psi}^*(s\omega)G(k,\omega)e^{-i\omega\tau}d\omega \qquad (2)$$

where $\widehat{\psi}$ denotes the FT of ψ in time and $G(k,\omega) = (2\pi)^{-3/2}\int_0^{2\pi} dx \int_{-\infty}^{\infty} g(x,t)e^{ikx}e^{i\omega t}dt$.

The performance of the WT depends on the choice of the mother wavelet and it should be made based on the nature of the signal and the purpose of application (e.g., Addison 2002). There exist a wide variety of mother wavelets to choose from for use, as any oscillatory mathematical function that is confined in both time and frequency and satisfies the so-called "admissibility condition" [i.e., $\widehat{\psi}(0) = 0$] could be a mother wavelet. In many geophysical applications, however, the Morlet wavelet has been used most extensively because of its similarity with trigonometric functions and thus the wavelet scale can be well related to the Fourier timescale (Meyers et al. 1993) that we are accustomed to. For this reason, we limit ourselves solely to the complex Morlet mother wavelet in this study. Note that the mother wavelet must be complex to express both eastward and westward propagating components (see Fig. 1).

The complex Morlet wavelet is given by

$$\psi(t) = e^{i\omega_0 t}e^{-t^2/2} \qquad (3)$$

and its FT (i.e., in the frequency domain)

$$\widehat{\psi}^*(\omega) = e^{-1/2(\omega_0-\omega)^2} \qquad (4)$$

where $|\omega_0|$ is usually set to 6 to ensure that the admissibility condition approximately holds (Farge 1992). Meyers et al. (1993) derived the relationship between the Morlet wavelet scale and the Fourier frequency by considering how a sinusoidal wave is represented by the Morlet WT

$$s = \frac{\omega_0 + (\omega_0^2 + 2)^{1/2}}{4\pi f} \qquad (5)$$

where $f = \omega/2\pi$ is Fourier frequency.

As in the one-dimensional WT and FT, the CFWT is invertible (i.e., the original signal can be exactly reconstructed). Because of the redundancy of the continuous WT, there exist many different reconstruction formulas (Farge 1992). Yet because of its simplicity, we use the following formula making use of the Dirac delta function (the proof of a reconstruction formula can be found in a text such as Marrat 2008)

$$g(x,t) = \frac{1}{C_\delta} \sum_{k=-\infty}^{\infty} \int_{-\infty}^{\infty} (\mathcal{T}g)(k,s,t)e^{-ikx}\frac{ds}{|s|^{3/2}} \qquad (6)$$

where $C_\delta = \sqrt{2\pi}\int_{-\infty}^{\infty}|\widehat{\psi}(\omega)|/\omega d\omega$. From this reconstruction formula, a spatial–temporal filter may be defined

$$g'(x,t) = \frac{1}{C_\delta} \sum \int_D (\mathcal{T}g)(k,s,t)e^{-ikx}\frac{ds}{|s|^{3/2}} \qquad (7)$$

where $D = \{(k,s) \in \mathbb{R}^2\}$ defines the region of summation and integration, and $g'(x,t)$ is the filtered signal that retains the particular spatial–temporal scales of interest determined by D.

Another important property of the CFWT is energy conservation, namely the total energy of the signal in the space–time domain is equal to that in the spectral domain (i.e., Parseval's relation)

$$\frac{1}{C_\psi} \sum_{k=-\infty}^{\infty} \int_{-\infty}^{\infty} \frac{ds}{s^2} \int_{-\infty}^{\infty} |(\mathcal{T}g)(k,s,\tau)|^2 d\tau$$

$$= \int_{0}^{2\pi} dx \int_{-\infty}^{\infty} |g(x,t)|^2 dt = 2\pi \sum_{k=-\infty}^{k=\infty} \int_{-\infty}^{\infty} |G(k,\omega)|^2 d\omega \quad (8)$$

where $C_\psi = \int_{-\infty}^{\infty} d\omega \left|\widehat{\psi}(\omega)\right|^2 / \omega$.

We define a *local power spectrum* P (often referred to as a scalogram in the WT literature) that measures the local energy of g at a given time, as a function of zonal wavenumber and wavelet scale

$$P(k,s,t) = |(\mathcal{T}g)(k,s,t)|^2 \quad (9)$$

The averaged power spectrum over a period from $t = t_1$ to $t = t_2$ is defined as

$$\bar{P}(k,s) = \int_{t_1}^{t_2} P(k,s,\tau)/(t_2 - t_1) d\tau \quad (10)$$

The *global power spectrum* is defined as its extreme case in which the averaging period corresponds to the entire data period.

2.2 Consideration of practical applications

We briefly discuss some practical issues that arise when applying the CFWT to real data, on the basis in large part of the discussion of Torrence and Compo (1998). Without loss of generality we can assume that the data is discrete, zonally periodic, and finite in time. A discretized form of the continuous CFWT (2) can be obtained by discretizing the wavelet scale such that $s = s_0 2^{j\delta_j}, j \in \mathbb{N}^0, j = 0, 1, \ldots, J$, and $s_0, \delta_j \in \mathbb{R}$. The values of s_0 and J should be chosen to cover the entire timescales of interest.

To minimize end effects (i.e., wrap-around pollution), the data is padded with enough zeros in such a way that the data length in time becomes a power of two for the computational efficiency of the fast FT. In addition, the CFWT spectra within the distance of the cone of influence ($\sqrt{2}s$ for the Morlet wavelet) from either end are excluded from analysis.

By analogy with the one-dimensional WT and FT, the sampling distribution of the CFWT power spectrum is expected to be the Chi square (χ^2) distribution with v degrees of freedom (DOF). For a local spectrum estimate (P) $v = 2$ and for a composite spectrum estimate consisting of n independent samples $v = 2 \times n$. While for an
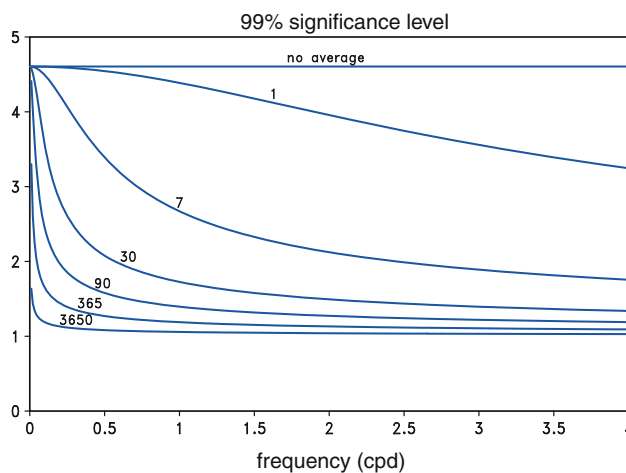

Fig. 2 Normalized 0.99 quantiles of the Chi square distribution $(\chi_v^2(0.99)/v)$ yielding the 99 % significance level for averaged spectrum estimates (10) with $n_a \delta_t$-day averages as indicated as a function of frequency. It is assumed that $\delta_t = 0.125$ day, v is given by (11), and the averaged spectrum estimates are normalized by a background spectrum

averaged spectrum estimate ($\bar{P}$) over a period of time $n_a \delta_t$ [i.e., $t_2 - t_1$ in (10)]

$$v = 2\sqrt{1 + \left(\frac{n_a \delta_t}{\gamma s}\right)^2} \quad (11)$$

where n_a is the number of averaging points, δ_t is the time resolution of the data, and the decorrelation factor (related to serial correlation in the WT spectrum) $\gamma = 2.23$ for the Morlet mother wavelet. The formula (11) as well as the γ value was derived by Torrence and Compo (1998) based on a Monte Carlo simulation assuming a white noise process.

The frequency-dependent nature of v in an averaged CFWT spectrum would not complicate statistical handling too much, especially when the averaging period is relatively large. Figure 2 shows the normalized 0.99 quantiles of the Chi square distribution $(\chi_v^2(0.99)/v)$ for averaged spectrum estimates with different $n_a \delta_t$, yielding the 99 % significance level at which normalized spectral peaks stand out significantly from the background spectrum. Since, according to the Central Limit Theorem, the Chi square distribution approaches the Gaussian distribution as the DOF increases, the normalized quantile converges to a certain value for large DOF. In fact, for sufficiently large n_a, the 99 % significance level is approximately the same over a reasonably wide range of frequencies, except in the vicinity of $f = 0$ cycle per day (cpd). Thus, in the following presentation where n_a is relatively large, we use the same contour levels across all frequencies.

3 Application to CLAUS data

This section demonstrates how the CFWT works by showing a series of examples through its application to tropical convection with particular emphasis on CCEWs. As a proxy for deep convection, brightness temperature (T_b) data from the cloud archive user service (CLAUS) (Hodges et al. 2000) was used for the period July 1983–June 2006 (23-year length). The data is available globally on a 3-hourly, $0.5° \times 0.5°$ longitude–latitude grid with few missing values within the tropics.

Prior to spectral analysis, some pretreatment processes were carried out. Missing data values were filled by temporal linear interpolation. To prewhiten the data, the linear trend and obvious frequency components that include the three harmonics of the climatological annual cycle and climatological diurnal cycle were removed at each grid point. The data was then separated into equatorially symmetric and antisymmetric components.

The CFWT power spectrum was computed by means of the discretized version of (2), as discussed in the previous section, with $w_0 = 6$, $s_0 = 0.22$ day, and $J = 44$, $\delta_j = 0.2$ at each latitude between 15°S and 15°N for the symmetric and antisymmetric components, separately. In the interest of simplicity, our arguments are based on averaged spectra over that latitudinal range. The choice of the latitudinal range is in line with many previous studies (e.g., Wheeler and Kiladis 1999; Kiladis et al. 2009; Yasunaga and Mapes 2012), and it follows from the geographical distributions of cloudiness variance associated with various types of CCEWs (e.g., Fig. 5 of Kiladis et al. 2009) that much of the variance is confined to that latitudinal band except for equatorial Rossby (ER) waves.

In order to make the method more practically feasible, we developed an elaborate method of representing the CFWT spectrum as well as estimating the background noise spectrum (see the "Appendix" for details). The here developed *frequency-dependent*, in place of *wavelet scale-dependent*, representation of the WT spectrum makes a comparison between the CFWT spectrum and the FT spectrum quite straightforward. In this representation we can readily apply existing techniques for estimating the background spectrum, an integral part of spectral analysis, that have been extensively developed in the context of FT-based spectral analyses. Taking advantage of it, we developed an objective approach to estimating the background spectrum for the CFWT spectrum based on a stochastic model for a time series. Close inspection indicates in isolating significant spectral peaks that the background spectrum obtained in our method leads in the lower frequency range up to ~ 0.5 cpd to results in relatively good agreement with the conventional ad hoc approach

introduced by Wheeler and Kiladis (1999), while in the higher frequency range it tends to highlight peaks associated with inertio-gravity (IG) waves, resulting in the identification of significant peaks even at frequencies as high as 2 cpd or more. Divergence in the background spectrum estimate between studies is in large part due to our incomplete knowledge of the underlying stochastic process that generates the observed space–time series. In other words, a proper framework does not yet seem to exist for estimating the background noise spectrum in a space–time series. Given the instrumental role of the background spectrum in spectral analysis, this issue deserves further research. Our objective approach, however, provides an arguably reasonable means of estimating the background spectrum on the basis of a stochastic model for a time-series and would be valid to the extent that the noise spectrum in the time series of each zonal wavenumber is well approximated by such a stochastic model.

3.1 Comparison between the CFWT spectrum and the FT spectrum

To see how the CFWT works, we begin with a comparison of the climatological-mean (global) spectrum estimates based on the CFWT and the FT, as shown in Fig. 3. The comparison reveals a remarkable level of agreement between the CFWT and the FT spectra, while the CFWT spectra yield more smeared appearance. This is in consistent with the view that the WT could be understood in terms of a modified (or in a way optimized) version of the short time (windowed) FT with the window length varying with the timescale of interest (e.g., see Addison 2002). As a result, according to the Heisenberg uncertainty principle (i.e., trade-off between time localization and frequency localization), the CFWT has lower (higher) frequency resolutions at higher (lower) frequencies. Thus smearing is more apparent at higher frequencies.

Consistent with previous studies, significant peaks, in the frequency range up to 0.9 cpd, are found along the theoretical dispersion curves for certain types of equatorial waves with equivalent depths of 8–50 m based on shallow water equations on an equatorial β plane: Kelvin, $n = 1$ ER, $n = 1$ westward inertio-gravity (WIG) waves in the symmetric component and $n = 0$ eastward inertio-gravity (EIG), mixed Rossby-gravity (MRG), and $n = 2$ WIG waves in the antisymmetric component (note that the MRG peak at around zonal wavenumber 0 seen in the FT spectrum does exist in the CFWT spectrum, but it is not seen with the contour levels used). Also found in both symmetric and antisymmetric components are weak, but significant westward propagating signals outside the pure equatorial wave modes that are usually referred to as
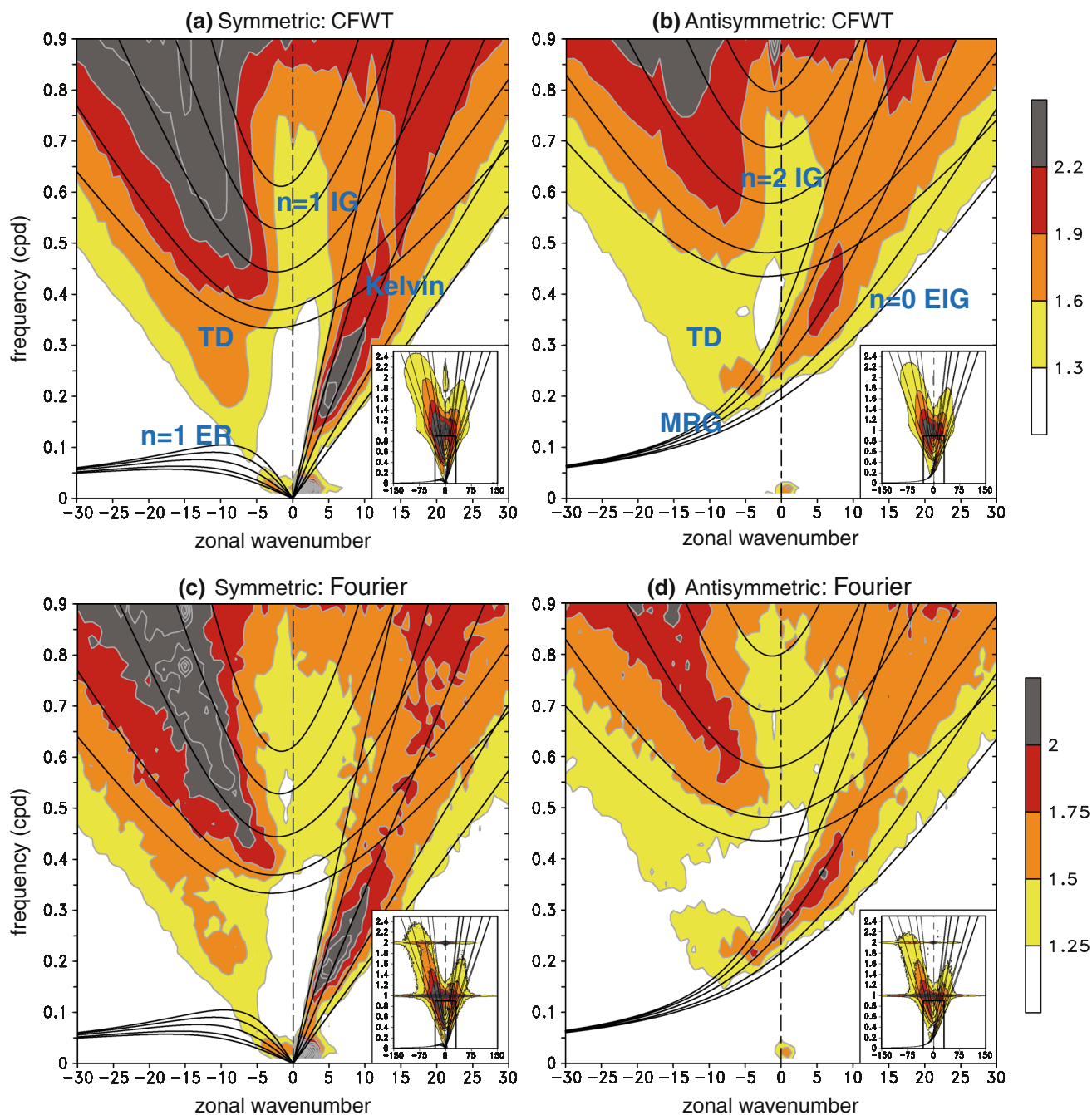
Fig. 3 Zonal wavenumber-frequency power spectrum estimates of CLAUS T_b for July 1983–June 2006 for the equatorially symmetric (*left panels*) and antisymmetric (*right panels*) components based on the CFWT (*top panels*) and FT (*bottom panels*) methods. Each spectrum is the average over 15°S–15°N and normalized by the red noise background power spectrum obtained in the manner explained in the "Appendix". A conservative estimate of the DOF for the Fourier-based power spectra is ∼524 [2(sine and cosine) × 23(year) × 365(days) × 3(smoothing)/96(segment length)], while that for the CFWT is a function of frequency [increases almost linearly with frequency, see (11)] and is expected to have the same DOF value as for the FT spectra at $f \sim 0.07$ cpd. The normalized power spectrum with that DOF larger than or equal to 1.15 is significantly greater than the background power spectrum at the 99 % level. Solid curves denote dispersion curves for the Kelvin, n = 1 equatorial Rossby (ER), n = 1 and n = 2 westward inertio-gravity (WIG), n = 0 eastward inertio-gravity (EIG), and mixed Rossby-gravity (MRG) waves with equivalent depths of 8, 12, 25, 50, and 90 m. The inset in the lower right corner of each panel shows a wider wavenumber-frequency range

tropical depression (TD)-type disturbances (Takayabu and Nitta 1993) characteristic of 2–6 day periodicity and zonal wavenumbers greater than 6 (Kiladis et al. 2006). The appearance of the signal in both components reflects the fact that convective anomalies associated with TD-type waves tend to appear only on either side of the equator at a time (e.g., Serra et al. 2008).

Significant signals are found even at higher frequencies along the dispersion curves for n = 1 and n = 2 IG waves, with westward propagating components being much stronger. Sharp spectral peaks appear at the diurnal and semidiurnal frequencies in the FT spectra, while the corresponding peaks are much more smeared in the CFWT counterpart. The significant diurnal and semidiurnal peaks probably owe their existence to the fact that diurnal cycles are strongly modulated by the MJO (e.g., Chen and Houze 1997; Tian et al. 2006), despite the removal of the climatological diurnal cycle as discussed above. The appearance of the significant signals in the higher frequencies is in consistent with a recent study by Tulich and Kiladis (2012) that analyzed the Tropical Rainfall Measuring Mission (TRMM) precipitation product (3B42) of the same time resolution (3-h).

In conclusion, the CFWT provides reasonable instantaneous spectrum estimates over a wide range of space–time scales in the sense that when averaged over a long period of time the averaged spectrum exhibits remarkable agreement with the FT spectrum estimate for the same period. In addition, the frequency-dependent representation of the CFWT spectrum developed in this study works very well.

3.2 Annual cycle

Much of what we know about the annual variations of CCEWs is based on FT-based analyses. Using cloudiness or precipitation data, the annual variations of CCEWs have been described in terms of seasonal-mean space–time spectra (e.g., Cho et al. 2004; Masunaga 2007) and/or the geographical distributions of seasonal or monthly mean variance of space–time filtered fields for various CCEW components (e.g., Roundy and Frank 2004; Huang and Huang 2011). Despite all these efforts, our knowledge remains limited due, in large part, to the limitations of the FT. More specifically, how the space–time spectral properties of CCEWs vary over the course of the year is little known in detail. This subsection demonstrates how such non-stationary spectral properties associated with the annual cycle can be obtained by means of the CFWT.

It is nonetheless instructive to start by considering climatological seasonal-mean spectra. As in common practice in WT analysis, the seasonal-mean spectra were normalized by the same background spectrum used in Fig. 3 (the validity of the use of a global spectrum-derived

background spectrum was argued in Torrence and Compo 1998). In analogy with the climatological-mean spectra (Fig. 3), the CFWT spectra agree well with the FT counterparts (not shown). It is evident from Figs. 4 and 5 that both symmetric and antisymmetric components exhibit pronounced annual variations. Eastward propagating disturbances in both components are substantially suppressed at overall frequencies during boreal summer, whereas they are most enhanced during spring. On the other hand, westward propagating disturbances tend to be suppressed during the winter and most enhanced from the spring to fall seasons, depending on the component. The striking annual cycle seen in the higher frequencies of ≥0.9 cpd as well as in the lower frequencies may have profound influence on the seasonal dependence of the QBO (Dunkerton 1990; Gabis and Troshichev 2011) through their role as an energy source in regulating the strength of vertically propagating waves into the stratosphere. Since the latitudinal range used to compute the spectra may not be wide enough for ER waves, as mentioned earlier, the remainder of this subsection is not concerned with ER waves.

With the CFWT, the annual variations of CCEWs can be examined in greater detail in terms of the space–time spectrum. Figure 6 compactly shows how the spectrum of CCEWs varies with the annual cycle in the form of predominant spectral peaks as a function of time and frequency stratified by symmetric/antisymmetric and eastward/westward propagating component. It is evident that all the CCEW components except for MRG and TD-type waves have double peaks through the annual cycle interspersed with relatively inactive periods in summer and winter: the primary peak in boreal spring and the secondary in winter, which reflects the asymmetry of the annual cycle in the ITCZ (e.g., Mitchell and Wallace 1992; Waliser and Gautier 1993). The primary peak is stronger and more extensive, indicating those CCEWs tend to be pronounced on a range of space–time scales. Boreal summer provides a special environment that suppresses the aforementioned CCEW types, especially those propagating eastward (Fig. 6b, d), but enhances TD-type and/or MRG waves (Fig. 6c), of which significant signals can be viewed as more like MRG waves at lower frequencies and as more like TD-type waves at higher frequencies, as inferred from Fig. 5c.

It is useful to examine how the climatological-mean statistics discussed above are shaped by individual convective events to gain some insights into the nature of CCEWs. Figure 7 provides an example of such analysis for the case of the 2001 JJA. Here we focus on the antisymmetric component, in particular MRG and TD-type waves (collectively referred to as MRG-TD-type waves), whose cloudiness variance tends to be concentrated in the ITCZ over the Pacific (e.g., see Fig. 5 of Kiladis et al. 2009),
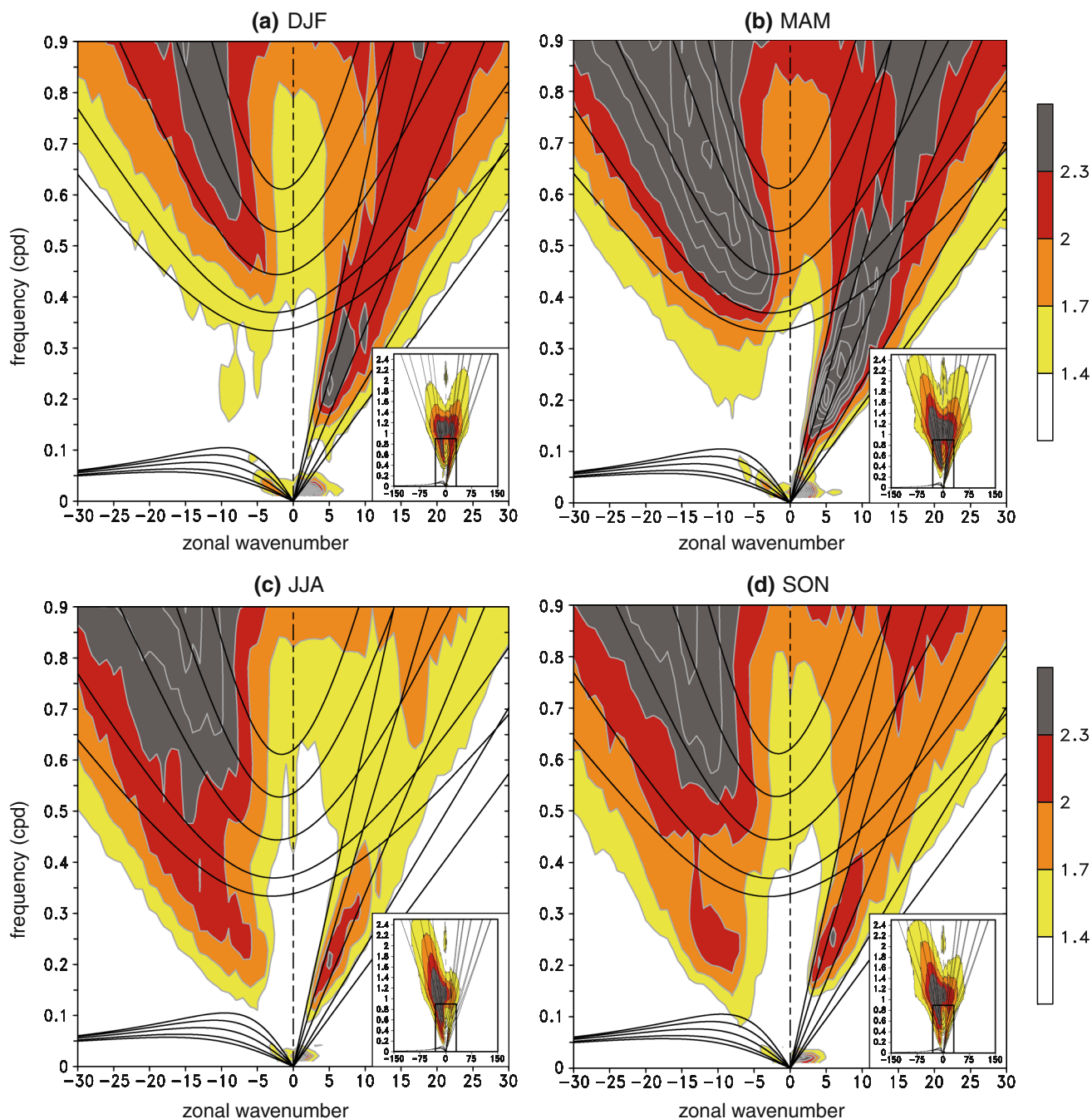
Fig. 4 As in Fig. 3a, but for **a** December–February, **b** March–May, **c** June–August, and **d** September–November mean. The same background spectrum as in Fig. 3a was used for normalization. *Note* that the DOF is estimated to be $\sim 2\sqrt{1 + \left(\frac{n_a \delta_t}{\gamma s}\right)^2} \times 23(\text{year})$. For instance, $n_a \delta_t = 91$ for MAM and the 99 % significant level at $f = 0.07$ is ~ 1.3

corresponding roughly to the longitudinal range of the figures. Climatologically speaking, the JJA season may be divided into two distinctive periods: the first half is marked by the presence of significant eastward propagating signals at lower frequencies (Fig. 6b, d) and the latter by their complete absence and the presence of significant MRG-

TD-type wave signals (Fig. 6a, c). These climatological features hold even for the 2001 JJA case; for example, the first half was marked by the predominance of eastward propagating cloudiness envelopes that correspond to Kelvin waves, whereas such envelopes were not pronounced in the second half (Fig. 7a). Note that the presence of the
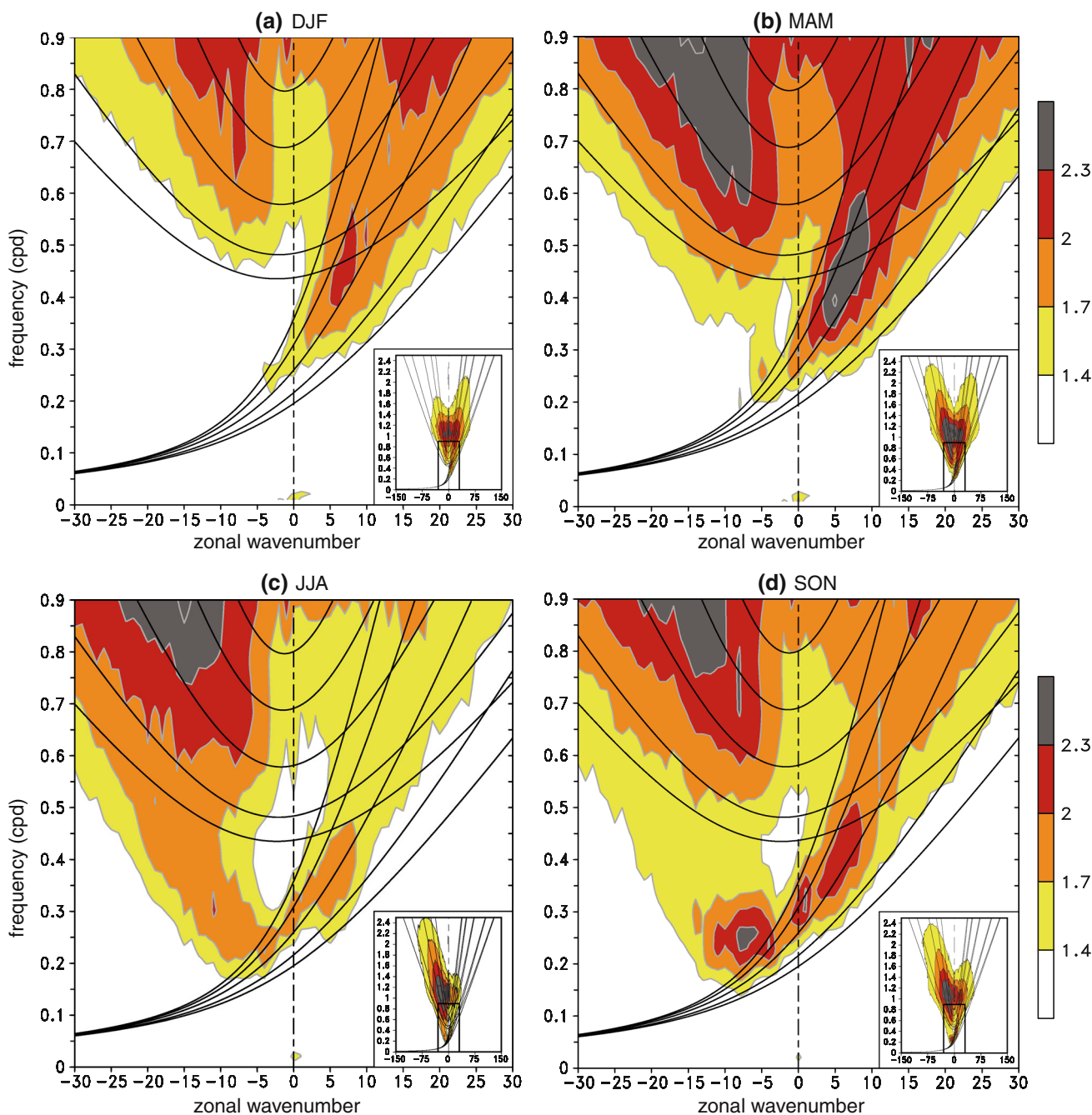
Fig. 5 As in Fig. 3, but for the antisymmetric component

Kelvin wave signals even in the antisymmetric component reflects the fact that the ITCZ is located far north of the equator.

Of particular interest are changes in the behavior of MRG-TD-type waves over the course of the JJA. In the first half vigorous MRG-TD-type wave activity was mainly concentrated in the western part of the Pacific, whereas it was slightly more widespread over the entire Pacific in the second half (Fig. 7b). Most of the MRG-TD-type waves in

June appeared to develop in association with the Kelvin wave envelopes, whereas the association of the MRG-TD-type waves in the other period with any well-defined larger scale systems may not be evident. Among the most striking features is the change in the spectral properties of the MRG-TD-type waves (Fig. 7c): the characteristic time-scales of the MRG-TD-type waves in early June (∼0.2 cpd) are longer than those in late July (∼0.35 cpd). The difference in the spectral properties of the MRG-TD-

Fig. 6 Climatological annual
cycle of the normalized power
spectrum of the symmetric
a westward and **b** eastward
propagating component and the
antisymmetric **c** westward and
d eastward propagating
component in terms of the peak
values over the entire negative
(westward) or positive
(eastward) zonal wavenumbers,
plotted as a function of season
and frequency. *Note* that the
99 % significance level is
~1.55 with 46 [2(sine and
cosine) × 23(year)] DOF. The
mode that corresponds to
spectral peaks at certain
frequencies is indicated on the
right
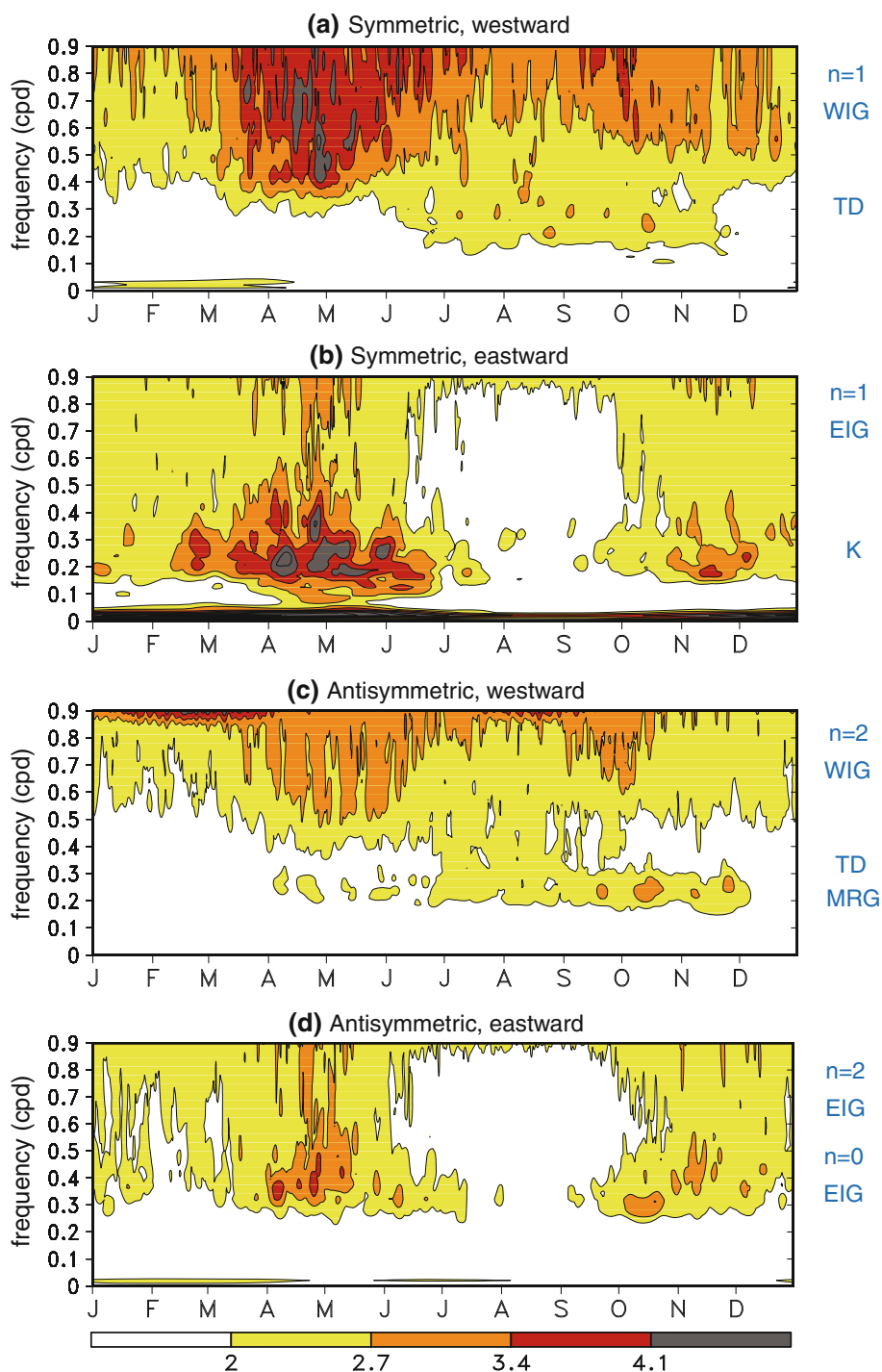
type waves is more apparent in the averaged space–time spectra over the two contrasting periods shown in Fig. 7d, e. Significant TD-MRG-type signals in early June are mostly oriented along the dispersion curve for the MRG wave mode even at smaller zonal scales, whereas they are in the TD-type wave range in late July.

Further analysis is beyond the scope of this study, although it is worth discussing some issues surrounding

MRG-TD-type waves. Because of their profound influence on tropical cyclone genesis (e.g., Frank and Roundy 2006; Schreck et al. 2012), a comprehensive understanding of them is of both scientific and practical importance. In fact, nearly all of the tropical depressions shown in Fig. 7b appeared to form in association with these wave modes in some way. Still, our current understanding of the underlying dynamical and physical processes of MRG-TD-type

Fig. 7 Behavior of CCEWs associated with the antisymmetric component in 2001 boreal summer. **a** Time–longitude section of meridionally averaged antisymmetric T_b anomalies between 15°S–15°N, **b** as in **a** but for MRG-TD-type wave filtered T_b anomalies in the foreground and the total antisymmetric anomalies in the background, **c** peak values of the westward propagating antisymmetric component within the range of zonal wavenumbers −1 to −20 as a function of frequency and time, and **d**, **e** averaged power spectrum of the antisymmetric component over the period I and the period II, indicated by the *bold dashed boxes* in **c**, respectively. In **a**, *dotted arrows* indicate Kelvin waves. In **b** MRG-TD-type wave filter was defined as a *rectangular* filter that passes signals having zonal wavenumbers of 1–20 and frequencies of 0.1–0.5 cpd and the contour interval is 4 W m^{-2} and the zero contour is suppressed. Tropical cyclone symbols are superimposed to depict tropical depression formation, defined as the maximum sustained wind speed first reaching 25 knots according to the Joint Typhoon Warning Center best track data. In **c** $v = 2$ everywhere and the 99 % significance level is ~4.6. In **d**, **e** v increases with frequency and $v = 3$ at $f \sim 0.1$ and the 90 % significance level with that ~2.1
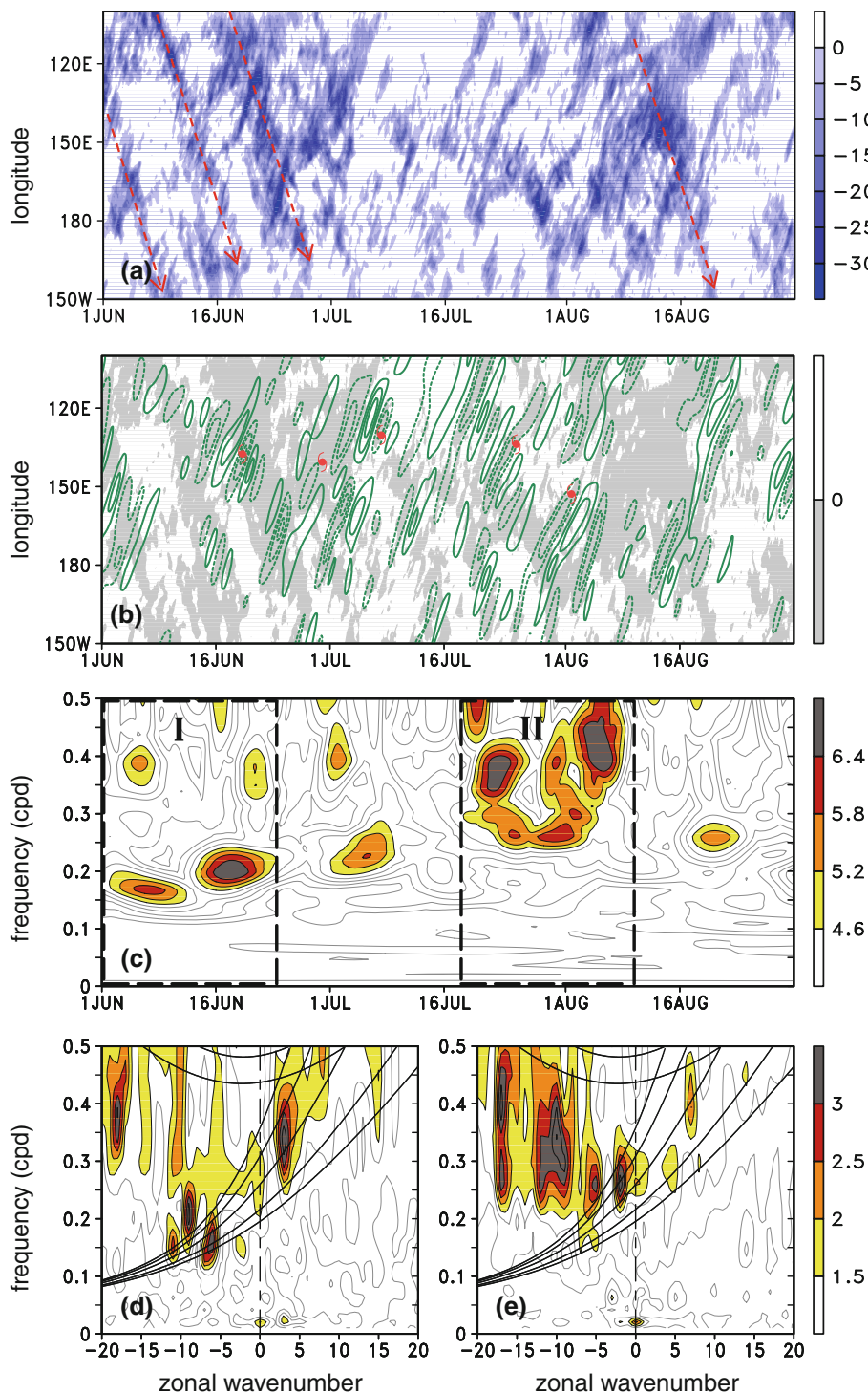
waves remains unsatisfactory, presumably reflecting the fact that these wave modes develop in a slowly varying, complicated, inhomogeneous summertime background environment, in which horizontal and vertical shear, and sea surface temperature are among the critical factors. Thus it seems natural that the properties, such as space–time scales and horizontal structure, of MRG-TD-type waves appear to depend strongly on the geographical location (i.e., as a function of longitude) in which they evolve (e.g., Liebmann and Hendon 1990; Dunkerton and Baldwin 1995). For example, in a typical summertime situation, MRG waves with longer wavelengths of 6,000–10,000 km tend to be preferred over the central Pacific, whereas TD-type waves with shorter wavelengths of 2,000–6,000 km in the western Pacific. Transition from MRG waves to TD-type waves over the western Pacific (e.g., Takayabu and

Nitta 1993; Dickinson and Molinari 2002) is perhaps a good manifestation. Such typical longitude-dependent property selection presumably shapes the climatological summertime mean spectrum (Fig. 5c). Our results, however, indicate that the property selection rule may drastically change from one period to another. Namely, there are times when the MRG wave mode is almost exclusively preferred at overall zonal scales (i.e., probably at overall longitudes) and that situation tends to occur more frequently only in early summer and late fall (not shown). At this point it is not clear whether the MJO contribute to it or not (Dias et al. 2013). The nonstationary features shown here warrant further studies to elucidate the underlying processes responsible for the selection rule determining MRG-TD-type wave properties.

3.3 Interannual variability: relationship with El Niño

We have seen that the statistical spectral properties of CCEWs vary greatly with the annual cycle. Such properties also vary from one year to the next. As a basis for understanding the year-to-year variations of CCEWs, this subsection considers those that occur in association with El Niño, by far the most prominent interannual variability in the tropics. Recently, Huang and Huang (2011) examined year-to-year variability of CCEWs based on monthly-mean wave activity using space–time filtered outgoing longwave radiation anomalies for several CCEW components, although there are relatively few previous works.

The capability of the CFWT to represent an instantaneous space–time spectrum readily enables us to examine possible links between CCEWs and El Niño without the use of space–time filtering techniques (i.e., no a priori assumption is made about the space–time structures of CCEWs). A statistical analysis based on linear lagged correlation, as shown in Fig. 8, reveals the existence of significant connections between convective activity associated with particular types of CCEWs and El Niño. It should be noted that the correlations were obtained without recourse to the background spectrum which played an integral role in identifying significant spectral peaks in previous figures. The types of CCEWs that are selectively modulated in activity include Kelvin, ER, relatively low-frequency eastward and westward propagating $n = 1$ IG waves, and high-frequency EIG waves in the symmetric part, and TD-type, low-frequency $n = 2$ WIG, low-frequency $n = 2$ or $n = 0$ EIG waves or both (peaks are found near regions in which the dispersion curves for $n = 0$ and 2 EIG waves asymptote), and high-frequency $n = 2$ EIG waves in the antisymmetric part. Of them only TD-type wave activity is negatively correlated with El Niño. The time lag at which their activity is most correlated with respect to El Niño varies gradually with zonal

wavenumber and frequency (bottom panels of Fig. 8). Kelvin, low-frequency $n = 0–2$ IG waves tend to be most enhanced at the height of El Niño (denoted by light orange shading), while ER and higher-frequency EIG waves tend to be most enhanced ~ 6 months before the peak of El Niño (denoted by dark blue shading). TD-type disturbances tend to be most suppressed ~ 2 months before the peak of El Niño.

To see how these changes as measured on a global scale are related to local changes in convective activity, Fig. 9 shows the patterns of regressed monthly-mean T_b variance for selected CCEWs along with regressed SST anomalies on Niño-3.4 index at selected lags. In the following discussion, we bear in mind that most El Niño events peak in December (e.g., Okumura and Deser 2010). At 6 months before the peak of El Niño, corresponding to a developing phase of El Niño, ER wave activity is enhanced over the western and central Pacific. Among the most pronounced features is a pair of variability peaks straddling the equator over the western Pacific with the northern peak being stronger, indicative of the preponderance of cyclonic ER gyres that produce westerly wind bursts (e.g., Vecchi and Harrison 2000; Seiki and Takayabu 2007), possibly facilitating subsequent development of El Niño through excitation of downwelling oceanic Kelvin waves (e.g., McPhaden 2008). The enhancement of ER waves may be understood in the context of the interaction between ER waves and the background environment as follows. ER waves can be more destabilized under the stronger easterly wind vertical shear condition (Wang and Xie 1996; Xie and Wang 1996) accompanied by the intensified and extended monsoon circulation in response to a seasonal-mean anomalous convective heating over the equatorial central Pacific during the developing phase of El Niño in boreal summer (e.g., Wu et al. 2009). At 2 months before the peak of El Niño, when overall TD-type wave activity tends to be most suppressed (Fig. 9b, d), the pattern of TD-type wave T_b variance is marked by a tripole structure, with enhanced activity over the equatorial central Pacific and suppressed activity over the western Pacific in both hemispheres. The change in the pattern of TD-type wave activity may be responsible in part for the southeastward shift in the genesis location of tropical cyclones observed during El Niño years (e.g., Chia and Ropelewski 2002; Wang and Chan 2002). Enhancements of Kelvin waves and low-frequency IG waves are evident in the ITCZ over the central and eastern Pacific at the height of El Niño. The enhancement of Kelvin waves that accompanies anomalous surface easterlies (e.g., Straub and Kiladis 2002) may, through excitation of upwelling oceanic Kelvin waves and/or amplification of preexisting those waves, contribute to relatively rapid decay of El Niño by next summer (e.g., Okumura and Deser 2010).
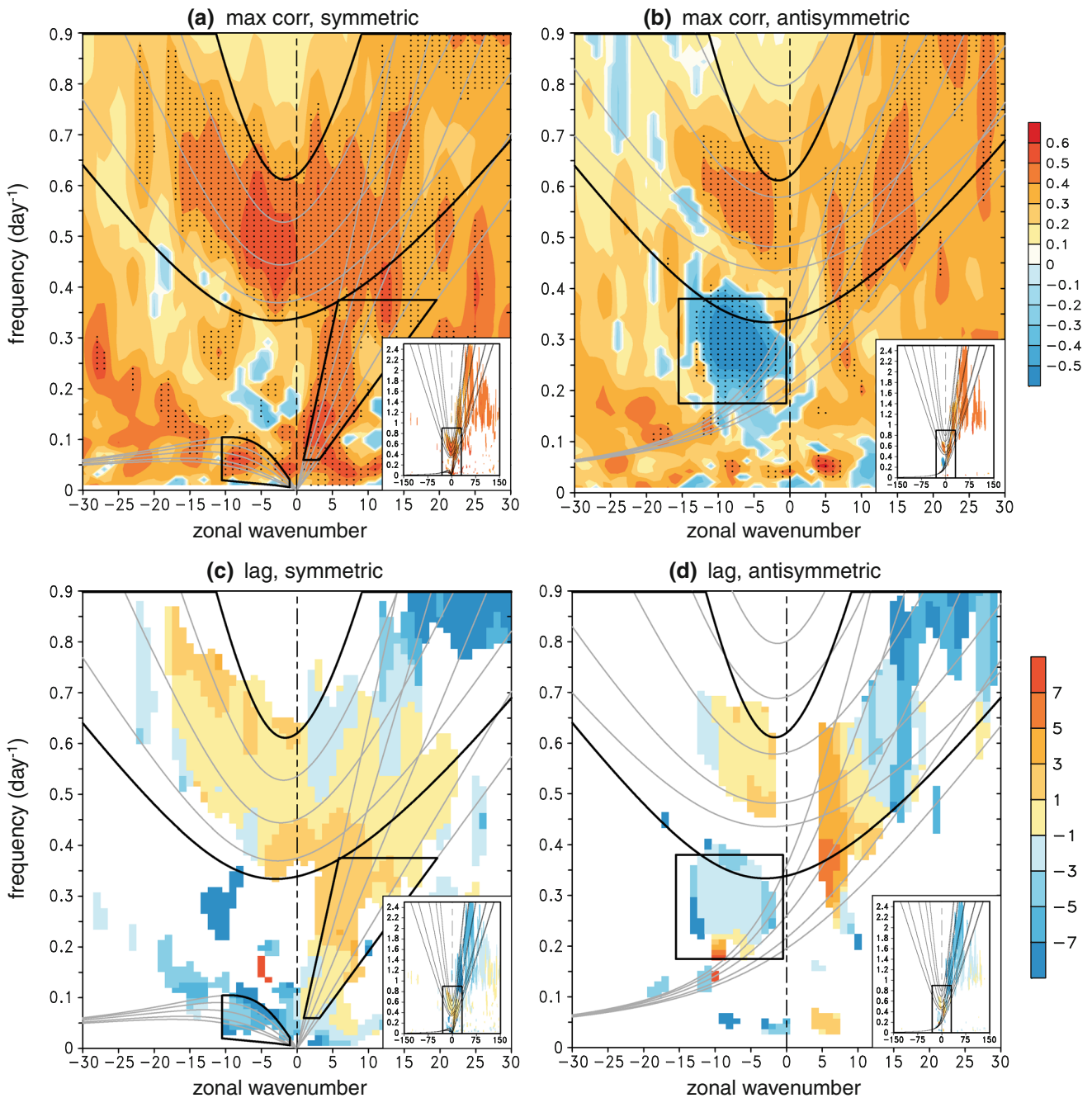
Fig. 8 *Top* Maximum lagged correlation coefficients between monthly-mean anomalies of CFWT power spectrum of CLAUS T_b at each frequency and zonal wavenumber and the monthly Niño-3.4 index, defined as SST anomalies in the region (5°N–5°S, 170°–120°W), and (*bottom*) the lags in months at which the maximum correlations take place. Prior to computing the correlation the (1-2-1)-filter (e.g., see von Storch and Zwiers 1999) was applied to the monthly-mean power spectrum in the zonal wavenumber direction two times for presentation purposes and 5-month running mean filter was applied to the monthly-mean power spectrum to suppress higher frequency oscillations. Stipple in the upper panels indicates where the correlation is statistically significant at the 95 % level, while in the lower panels and the insets values are shown only where correlations are significant at least at the 95 % level. In the significance test, reduction in the number of the effective sample size due to the presence of serial correlation (Davis 1976) was taken into account. In the *bottom* panels *blue* (*orange*) colors denote the power spectrum leads (lags) the Niño3.4 index. *Solid thick boxes* define the wavenumber-frequency regions used, by means of (7), for isolating the types of CCEWs to be used in calculating the regression maps in Fig. 9
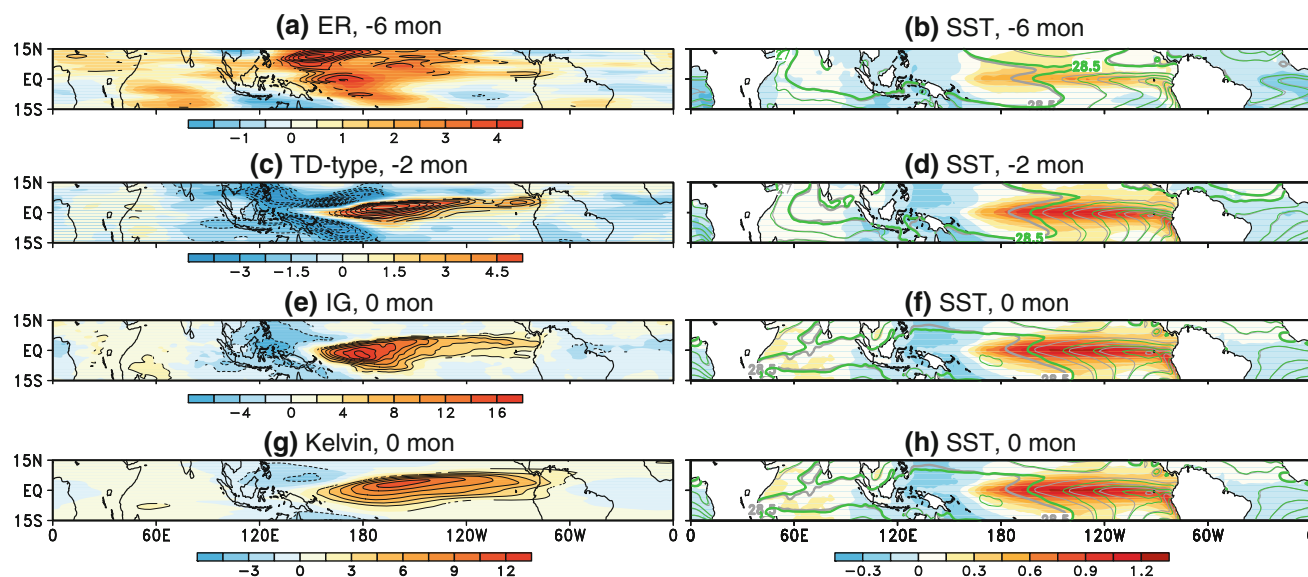
Fig. 9 *Horizontal* distribution of the regressed monthly-mean T_b variance of the **a** ER waves at −6 month lag, **b** TD-type waves at −2 month lag, **c** IG waves at 0 month lag, and **d** Kelvin waves at 0 month lag (*left*) and regressed SST (*color shading*) at the corresponding lags (*right*) onto the Niño3.4 index. Monthly-mean T_b variance for each wave type was calculated using the space–time filtered field that was obtained by means of (7), with each spectral characteristic defined by the corresponding box in Fig. 9. The 95 % significant level are only shown by contours (*left*). Contour interval in **a** 0.5, **b** 2, **c** 0.75, and **d** 1.5 (W m^{-2})^2. In the right panels, assuming that El Niño peaks in December as is the case for many El Niño events, the climatological monthly-mean SST is indicated by *gray* contours and the climatological monthly mean SST plus regressed SST anomalies are indicated by *green* contours. Contour interval 1 °C. Note that Niño3.4 anomalies are deviations from the 1981 to 2010 climatological mean values, while SST anomalies are deviations from July 1983 to June 2006 averages. SST data used is NOAA Optimum Interpolation SST V2 (Reynolds et al. 2002)

4 Conclusions

To better understand the nonstationary features of CCEWs, this study introduced a novel transform, referred to as the CFWT, defined as a combination of the Fourier series in space and the WT in time. The CFWT provides spatially global, temporary local spectral estimates, enabling us to describe temporal variations in the space–time spectrum. With the meticulous consideration of the representation and assessment of the CFWT spectrum made, we offer a standard package[1] based on the CFWT. The high level of agreement between the CFWT and FT in the climatological-mean space–time spectra allows us to conclude that the local CFWT spectrum is a reasonable snapshot, though the CFWT spectrum inevitably suffers from smearing due to the Heisenberg principle. The arguably reasonable estimate of the background red noise spectrum in an objective manner helps us detect significant CCEW signals on a wide range of space–time scales ranging in time from several hours to a few tens of days.

The time–frequency localization capability of the CFWT gives us an advantage relative to conventional FT-based approaches for studying weather-climate linkage.

The instantaneous space–time spectrum provided by the CFWT represents a "weather state" that can be interpreted to a great degree in terms of the superposition of CCEWs at a particular time and would serve as a basis for understanding the interrelationship between such weather state statistics and the more slowly varying atmosphere–ocean background state in which they are embedded. Through examinations of the annual cycle, interannual variability, and a case study, we demonstrated that the CFWT, in fact, provides a useful framework for illuminating how the properties of CCEWs can be regulated by the background state. Among the interesting features are the occasional occurrence of the background state in favor of MRG waves instead of TD-type waves even at small horizontal scales and the possibility of the interaction between CCEWs and El Niño. Regarding the interaction between El Niño and higher-frequency components, primary attention to date has been given to the MJO's role (e.g., Hendon et al. 2007; McPhaden 2008). Our results may suggest that CCEWs also contribute to regulating the onset and decaying timing of El Niño and call for further analysis.

The multiresolution nature inherent in the WT adds another advantage to the CFWT, especially when dealing with short-term record, even when its use is limited to detecting significant space–time spectral peaks. The multiresolution nature imparts differing DOF as a function of

---

[1] The program package will be available from the author's web site at www.soest.hawaii.edu/∼kazuyosh.

frequency, with larger DOF at higher frequencies, to the global CFWT spectrum. As a result, spectral peaks can be assessed over a wide frequency range with greater confidence relative to a FT-based method, though at the expense of frequency resolution (i.e., smearing). Of particular interest in its application are two periods corresponding to recent programs, Year of Tropical Convection (YOTC; Moncrieff et al. 2012; Waliser et al. 2012) and the international Cooperative Indian Ocean Experiment on Intraseasonal Variability in the Year 2011 (CINDY2011; http://www.jamstec.go.jp/iorgc/cindy/)/ The Dynamics of the MJO (DYNAMO; http://www.eol.ucar.edu/projects/dynamo/). Suppose, for example, that we analyze a three-month-long dataset (a situation similar to CINDY/DYNAMO). For a FT approach, assuming the segment length is equal to the length of the dataset and three passes of a smoothing filter in the spectral domain, v is estimated to be 6 everywhere. In contrast, for the CFWT, v is a function of frequency and $v \sim 6$ at $f = 0.07$ cpd and $v \sim 30$ at $f = 0.36$ cpd. This frequency-dependent nature of DOF would not complicate statistical assessment too much (Fig. 2).

In conclusion, the CFWT can be a useful tool in describing the nonstationary features of CCEWs. Although it is computationally more expensive by a few orders of magnitude relative to the conventional FT, it requires a few orders of magnitude less computational resources compared to the STWT (Kikuchi and Wang 2010) that is able to describe spatially as well as temporary localized variations in the space–time spectrum, rendering its application computationally more feasible and diagnostically easier to handle. The CFWT spectrum is spatially global, yet it reflects to a certain extent the local spectral characteristics over a particular region where the component in question is pronounced. Therefore, the CFWT can be still useful to those whose interests are limited to a particular region. In any case, the CFWT and the STWT, collectively, provide a comprehensive set of frameworks capable of documenting the nonstationarity in a space–time series with different levels of complexity (i.e., temporally localize or spatio-temporally localized).

Appendix: Representation of the CFWT spectrum and estimation of a red-noise background spectrum

Representation of the WT spectrum sometimes gives rise to confusion. The WT spectrum is usually represented as a function of wavelet scale and the wavelet scale is usually associated with Fourier frequency for analysis (e.g., Meyers et al. 1993). However, the WT spectrum in that representation is biased in magnitude toward higher frequencies (e.g., Telfer and Szu 1992; Liu et al. 2007), making direct comparison with the FT spectrum difficult. Figure 10 illustrates the situation for the case of the
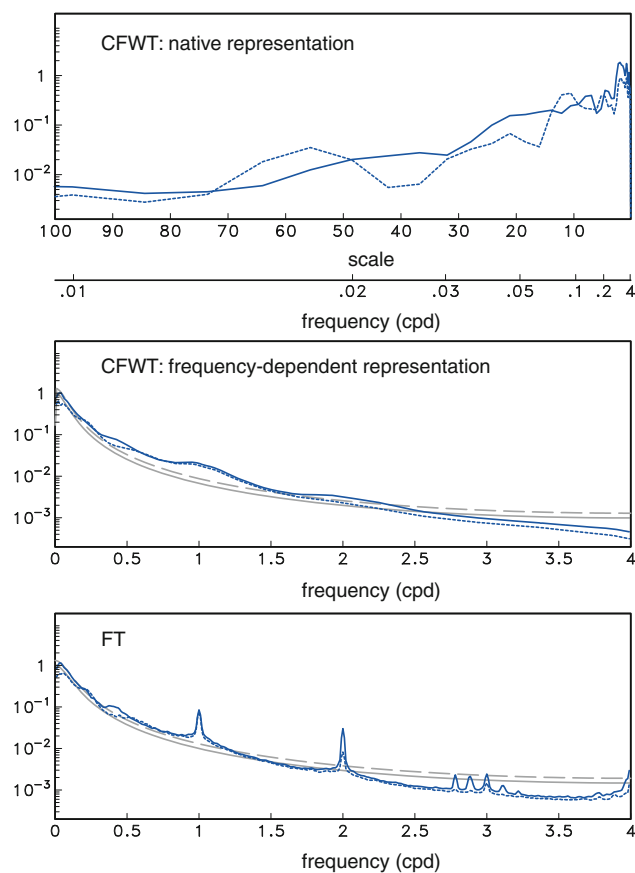

Fig. 10 Power spectrum estimates of T_b at zonal wavenumber -5. **a** Wavelet scale-dependent representation of the CFWT spectrum, **b** frequency-dependent representation of the CFWT spectrum, and **c** FT spectrum. Symmetric and antisymmetric components are denoted by *solid* and *dashed curves*, respectively. AR(1) red noise power spectra and their 1.3 times values are denoted by *gray solid* and *dashed curves*, respectively. Each spectrum is suitably scaled so that the maximum value is ~ 1

CFWT: the WT spectra of both the symmetric and anti-symmetric components at a particular zonal wavenumber (top panel) are blue (i.e., the spectrum increases with increasing frequency), while the FT counterparts are red (bottom panel).

In order to bridge the gap, we developed a method to convert the scale-dependent representation of the CFWT spectrum into a frequency-dependent representation. In light of energy conservation (8), the frequency-dependent spectrum $P(k, f_n)$ at discrete frequency f_n may be defined, making use of (5) and (9), as

$$|P(k, f_n, \tau)|^2 = \frac{1}{C_\psi} \int_{s_1}^{s_2} |(\mathcal{T}g)(k, s, \tau)|^2 \frac{ds}{s^2}$$

where $s_1 = \left[\omega_0 + (\omega_0^2 + 2)^{1/2}\right] \Big/ [2\pi(f_{n-1} + f_n)]$, $s_2 = \left[\omega_0 + (\omega_0^2 + 2)^{1/2}\right] \Big/ [2\pi(f_n + f_{n+1})]$. The resulting frequency-dependent CFWT power spectra (middle panel) are red and are in good agreement with the FT counterparts (bottom panel), yet they are somewhat smeared, resulting in more moderate peaks at the diurnal and semidiurnal frequencies.

Now, because of the similarity in appearance, we can anticipate that a technique that has been developed to assess FT space–time spectrum peaks is also applicable to the frequency-dependent CFWT spectrum. To determine the level of significance, we need to estimate the

background noise spectrum and DOF. Because we discussed how to estimate the DOF for the case of the CFWT in Sect. 2.2, we here focus on how to estimate the background spectrum. In contrast to the case of a one-dimensional time series, whose background noise is usually assumed to be generated by a process represented by a simple mathematical model (by the first-order autoregression AR(1) model for most geophysical time series), there is no consensus on how to estimate the background noise spectrum in a space–time series at this point. In their pioneering work, Wheeler and Kiladis (1999) defined the background spectrum by smoothing the total (i.e., sum of the symmetric and antisymmetric parts) raw spectrum in zonal wavenumber and in frequency many times. Recently, Masunaga et al. (2006) and Hendon and Wheeler (2008) developed a different approach by considering the fitting of the AR(1) model at each zonal wavenumber. This approach is arguably more objective than that of Wheeler and Kiladis (1999).

We took a similar approach but with more elaboration. To check the validity of model assumption, we considered three mathematical models including the power law distribution and bending power law distribution as well as the AR(1) model (for exact formulae see Vaughan et al. 2011). They together can represent a wide range of realistic noise spectra. At each zonal wavenumber the degree to which each model can fit to the total raw spectrum and the
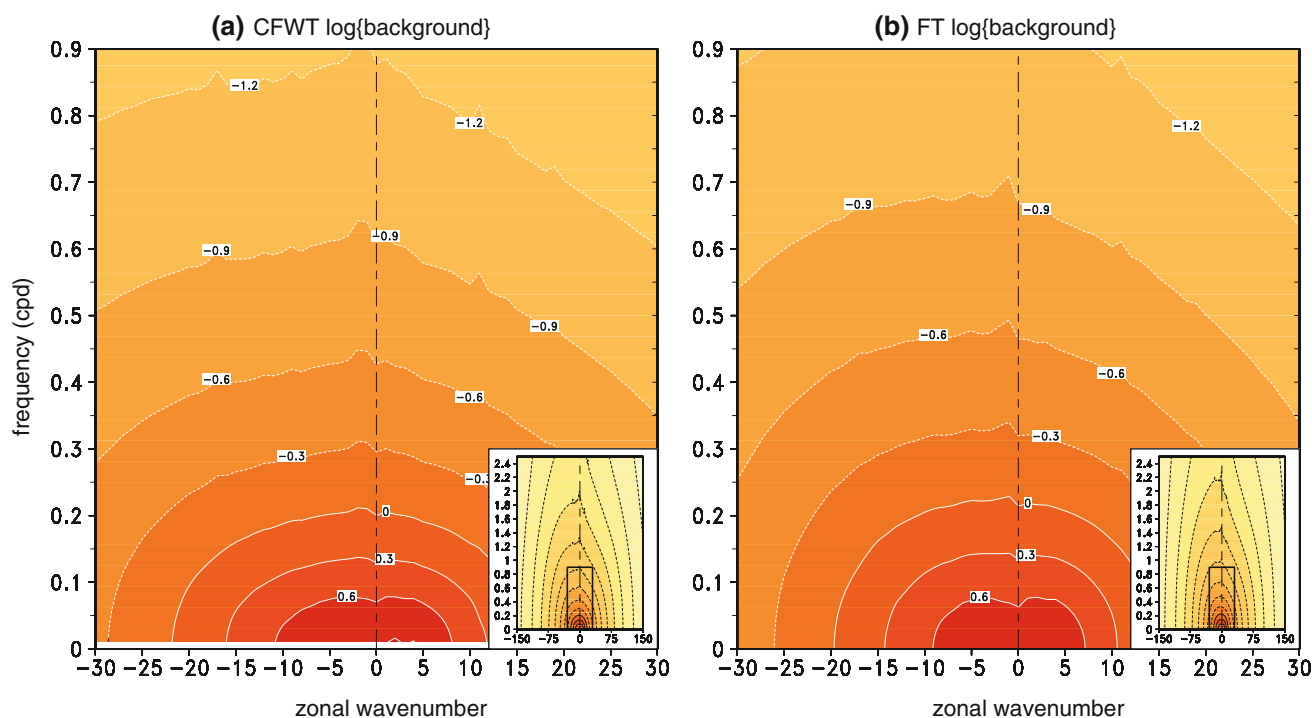

Fig. 11 Zonal wavenumber-frequency spectra of the base-10 logarithm of the background red noise power estimated by fitting the AR(1) model to the total raw spectrum for **a** CFWT and **b** FT

parameters of each model that provide best fit were determined by means of the maximum likelihood method (e.g., Stella et al. 1994). It was found that the AR(1) model fits best at nearly all the zonal wavenumbers within ∼ 160 for both the FT and CFWT global spectra (not shown).

Figure 11 shows the resulting background spectrum obtained based on the AR(1) model. Prior to the fitting of the AR(1) model, the power in the MJO spectral range (positive zonal wavenumbers 1–3 and frequencies up to 1/30 cpd) was halved in the total raw spectrum as with Hendon and Wheeler (2008). This treatment little affects the overall shape of the background spectrum. Clearly, both the CFWT and FT background spectra are to a large extent symmetric about zonal wavenumber 0 and highly red in both wavenumber and frequency.

References

Addison PS (2002) The illustrated wavelet transform handbook: introductory theory and applications in science, engineering, medicine and finance, 1st edn. Taylor & Francis, UK

Baldwin MP, Gray LJ, Dunkerton TJ, Hamilton K, Haynes PH, Randel WJ, Holton JR, Alexander MJ, Hirota I, Horinouchi T, Jones DBA, Kinnersley JS, Marquardt C, Sato K, Takahashi M (2001) The quasi-biennial oscillation. Rev Geophys 39:179–229

Chen SS, Houze RA Jr (1997) Diurnal variation and life-cycle of deep convective systems over the tropical Pacific warm pool. Q J R Meteorol Soc 123:357–388

Chia HH, Ropelewski CF (2002) The interannual variability in the genesis location of tropical cyclones in the northwest Pacific. J Clim 15:2934–2944

Cho HK, Bowman KP, North GR (2004) Equatorial waves including the Madden–Julian oscillation in TRMM rainfall and OLR data. J Clim 17:4387–4406

Davis RE (1976) Predictability of sea surface temperature and sea level pressure anomalies over the north Pacific ocean. J Phys Oceanogr 6:249–266

Dias J, Leroux S, Tulich SN, Kiladis GN (2013) How systematic is organized tropical convection within the MJO? Geophys Res Lett 40:1420–1425. doi:10.1002/grl.50308

Dickinson M, Molinari J (2002) Mixed Rossby-gravity waves and Western Pacific tropical cyclogenesis. Part I: synoptic evolution. J Atmos Sci 59:2183–2196

Dunkerton TJ (1990) Annual variation of deseasonalized mean flow acceleration in the equatorial lower stratosphere. J Meteorol Soc Jpn 68:499–508

Dunkerton TJ, Baldwin MP (1995) Observation of 3–6-day meridional wind oscillations over the tropical Pacific, 1973–1992: horizontal structure and propagation. J Atmos Sci 52:1585–1601

Duval-Destin M, Murenzi R (1993) Spatio-temporal wavelets: application to the analysis of moving patterns. In: Meyer Y, Roques S (eds) Progress in wavelet analysis and applications (Proc. Toulouse 1992). Frontières, Gif-sur-Yvette, pp 399–408

Farge M (1992) Wavelet transforms and their applications to turbulence. Annu Rev Fluid Mech 24:395–457

Frank WM, Roundy PE (2006) The role of tropical waves in tropical cyclogenesis. Mon Weather Rev 134:2397–2417

Gabis IP, Troshichev OA (2011) The quasi-biennial oscillation in the equatorial stratosphere: seasonal regularity in zonal wind changes, discrete QBO-cycle period and prediction of QBO-cycle duration. Geomag Aeron 51:501–512

Gu GJ, Zhang CD (2001) A spectrum analysis of synoptic-scale disturbances in the ITCZ. J Clim 14:2725–2739

Hendon HH, Wheeler MC (2008) Some space-time spectral analyses of tropical convection and planetary-scale waves. J Atmos Sci 65:2936–2948

Hendon HH, Wheeler MC, Zhang CD (2007) Seasonal dependence of the MJO-ENSO relationship. J Clim 20:531–543

Hodges KI, Chappell DW, Robinson GJ, Yang G (2000) An improved algorithm for generating global window brightness temperatures from multiple satellite infrared imagery. J Atmos Ocean Technol 17:1296–1312

Huang P, Huang RH (2011) Climatology and interannual variability of convectively coupled equatorial waves activity. J Clim 24:4451–4465

Hudgins L, Friehe CA, Mayer ME (1993) Wavelet transforms and atmospheric turbulence. Phys Rev Lett 71:3279–3282

Kawatani Y, Sato K, Dunkerton TJ, Watanabe S, Miyahara S, Takahashi M (2010) The roles of equatorial trapped waves and internal inertia-gravity waves in diving the quasi-biennial oscillation. Part I: zonal mean wave forcing. J Atmos Sci 67:963–980

Kikuchi K, Wang B (2010) Spatiotemporal wavelet transform and the multiscale behavior of the Madden–Julian oscillation. J Clim 23:3814–3834

Kiladis GN, Thorncroft CD, Hall NMJ (2006) Three-dimensional structure and dynamics of African easterly waves. Part I: observations. J Atmos Sci 63:2212–2230

Kiladis GN, Wheeler MC, Haertel PT, Straub KH, Roundy PE (2009) Convectively coupled equatorial waves. Rev Geophys 47:RG2003. doi:10.1029/2008RG000266

Kumar P, FoufoulaGeorgiou E (1997) Wavelet analysis for geophysical applications. Rev Geophys 35:385–412

Labat D (2005) Recent advances in wavelet analyses: Part I. A review of concepts. J Hydrol 314:275–288

Lau KM, Weng H (1995) Climate signal detection using wavelet transform: how to make a time series sing. Bull Am Meteorol Soc 76:2391–2402

Liebmann B, Hendon HH (1990) Synoptic-scale disturbances near the equator. J Atmos Sci 47:1463–1479

Liu YG, Liang XS, Weisberg RH (2007) Rectification of the bias in the wavelet power spectrum. J Atmos Ocean Technol 24:2093–2102

Marrat S (2008) A wavelet tour of signal processing, 3rd edn. Academic Press, Waltham

Masunaga H (2007) Seasonality and regionality of the Madden–Julian oscillation, Kelvin wave, and equatorial Rossby wave. J Atmos Sci 64:4400–4416

Masunaga H, L'Ecuyer TS, Kummerow CD (2006) The Madden–Julian oscillation recorded in early observations from the Tropical Rainfall Measuring Mission (TRMM). J Atmos Sci 63:2777–2794

Matsuno T (1966) Quasi-geostrophic motions in the equatorial area. J Meteorol Soc Jpn 44:25–43

McPhaden MJ (2008) Evolution of the 2006–2007 El Niño: the role of intraseasonal to interannual time scale dynamics. Adv Geosci 14:219–230

Meyers SD, Kelly BG, Obrien JJ (1993) An introduction to wavelet analysis in oceanography and meteorology: with application to the dispersion of Yanai waves. Mon Weather Rev 121:2858–2866

Mitchell TP, Wallace JM (1992) The annual cycle in equatorial convection and sea-surface temperature. J Clim 5:1140–1156

Moncrieff MW, Waliser DE, Miller MJ, Shapiro MA, Asrar GR, Caughey J (2012) Multiscale convective organization and the YOTC virtual global field campaign. Bull Am Meteorol Soc 93:1171–1187

Mounier F, Kiladis GN, Janicot S (2007) Analysis of the dominant mode of convectively coupled Kelvin waves in the West African monsoon. J Clim 20:1487–1503

Nakazawa T (1988) Tropical super clusters within intraseasonal variations over the western Pacific. J Meteorol Soc Jpn 66:823–839

Okumura YM, Deser C (2010) Asymmetry in the duration of El Nino and La Nina. J Clim 23:5826–5843

Reynolds RW, Rayner NA, Smith TM, Stokes DC, Wang WQ (2002) An improved in situ and satellite SST analysis for climate. J Clim 15:1609–1625

Roundy PE (2012) The spectrum of convectively coupled Kelvin waves and the Madden–Julian Oscillation in regions of low-level easterly and westerly background flow. J Atmos Sci 69:2107–2111

Roundy PE, Frank WM (2004) A climatology of waves in the equatorial region. J Atmos Sci 61:2105–2132

Roundy PE, Janiga MA (2012) Analysis of vertically propagating convectively coupled equatorial waves using observations and a non-hydrostatic Boussinesq model on the equatorial beta-plane. Q J R Meteorol Soc 138:1004–1017

Schreck CJ III, Molinari J, Aiyyer A (2012) A global view of equatorial waves and tropical cyclogenesis. Mon Weather Rev 140:774–788

Seiki A, Takayabu YN (2007) Westerly wind bursts and their relationship with intraseasonal variations and ENSO. Part I: statistics. Mon Weather Rev 135:3325–3345

Serra YL, Houze RA (2002) Observations of variability on synoptic timescales in the East Pacific ITCZ. J Atmos Sci 59:1723–1743

Serra YL, Kiladis GN, Cronin MF (2008) Horizontal and vertical structure of easterly waves in the Pacific ITCZ. J Atmos Sci 65:1266–1284

Stella L, Arlandi G, Tagliaferri G, Israel GL (1994) Continuum power spectrum components in x-ray sources: detailed modelling and search for coherent periodicities. In: Rao TS, Priestley MB, Lessi O (eds) Applications of time series analysis in astronomy and meteorology [arXiv:astro-ph/9411050v1]

Straub KH, Kiladis GN (2002) Observations of a convectively coupled Kelvin wave in the eastern Pacific ITCZ. J Atmos Sci 59:30–53

Takayabu YN (1994) Large-scale cloud disturbances associated with equatorial waves. Part I: spectral features of the cloud disturbances. J Meteorol Soc Jpn 72:433–449

Takayabu YN, Nitta T (1993) 3-5 day-period disturbances coupled with convection over the tropical Pacific Ocean. J Meteorol Soc Jpn 71:221–246

Telfer B, Szu HH (1992) New wavelet transform normalization to remove frequency bias. Opt Eng 31:1830–1834

Tian BJ, Waliser DE, Fetzer EJ (2006) Modulation of the diurnal cycle of tropical deep convective clouds by the MJO. Geophys Res Lett 33:L20704. doi:10.1029/2006GL027752

Torrence C, Compo GP (1998) A practical guide to wavelet analysis. Bull Am Meteorol Soc 79:61–78

Tulich SN, Kiladis GN (2012) Squall lines and convectively coupled gravity waves in the tropics: why do most cloud systems propagate westward? J Atmos Sci 69:2995–3012

Vaughan S, Bailey RJ, Smith DG (2011) Detecting cycles in stratigraphic data: spectral analysis in the presence of red noise. Paleoceanography 26:PA4211. doi:10.1029/2011PA002195

Vecchi GA, Harrison DE (2000) Tropical Pacific sea surface temperature anomalies, El Nino, and equatorial westerly wind events. J Clim 13:1814–1830

von Storch H, Zwiers FW (1999) Statistical anlysis in climate research. Cambridge University Press, Cambridge

Waliser DE, Gautier C (1993) A satellite-derived climatology of the ITCZ. J Clim 6:2162–2174

Waliser DE, Moncrieff MW, Burridge D, Fink AH, Gochis D, Goswami BN, Guan B, Harr P, Heming J, Hsu H–H, Jakob C, Janiga M, Johnson R, Jones S, Knippertz P, Marengo J, Hanh N, Pope M, Serra Y, Thorncroft C, Wheeler M, Wood R, Yuter S (2012) The "year" of tropical convection (May 2008–April 2010) climate variability and weather highlights. Bull Am Meteorol Soc 93:1189–1218

Wang B, Chan JCL (2002) How strong ENSO events affect tropical storm activity over the Western North Pacific. J Clim 15:1643–1658

Wang B, Xie X (1996) Low-frequency equatorial waves in vertically sheared zonal flow. Part I: stable waves. J Atmos Sci 53:449–467

Wheeler M, Kiladis GN (1999) Convectively coupled equatorial waves: analysis of clouds and temperature in the wavenumber-frequency domain. J Atmos Sci 56:374–399

Wong MLM (2009) Wavelet analysis of the convectively coupled equatorial waves in the wavenumber-frequency domain. J Atmos Sci 66:209–212

Wu B, Zhou T, Li T (2009) Seasonally evolving dominant interannual variability modes of east Asian climate. J Clim 22:2992–3005

Xie XS, Wang B (1996) Low-frequency equatorial waves in vertically sheared zonal flow. Part II: unstable waves. J Atmos Sci 53:3589–3605

Yang D, Ingersoll AP (2011) Testing the hypothesis that the MJO is a mixed rossby-gravity wave packet. J Atmos Sci 68:226–239

Yano JI, Moncrieff MW, Wu XQ, Yamada M (2001) Wavelet analysis of simulated tropical convective cloud systems. Part I: basic analysis. J Atmos Sci 58:850–867

Yasunaga K, Mapes B (2012) Differences between more divergent and more rotational types of convectively coupled equatorial waves. Part I: space-time spectral analyses. J Atmos Sci 69:3–16